J Mater Sci (2007) 42:6996–7003
DOI 10.1007/s10853-006-1185-2

Modeling of precipitation hardening in Mg-based alloys

Alexander Katsman · Shalom Cohen · Menachem Bamberger

Received: 9 April 2006 / Accepted: 26 October 2006 / Published online: 26 April 2007

Abstract This work deals with the development of Mg-based alloys with enhanced properties at elevated temperatures. This is achieved by precipitation of binary phases such as $MgZn_2$ and Mg_2Sn during the aging of these alloys. The aim of the present work is to develop and calibrate a model for precipitation hardening in Mg-based alloys, as different types of precipitates form simultaneously. The modified Langer-Schwartz approach, while taking into account nucleation, growth and coarsening of the new phase precipitations, was used for the analysis of precipitates' evolution and precipitation hardening during aging of Mg-based alloys. Two strengthening mechanisms associated with particle-dislocation interaction (shearing and bypassing) were considered to be operating simultaneously due to particle size-distribution. Parameters of the model, $R_N i$ and $k_{\sigma\ i}$, were found by fitting of calculated densities and average sizes of precipitates with ones estimated from experiments. The effective diffusion coefficients of phase formation processes, which determine the strengthening kinetics, were estimated from the hardness maximum positions on the aging curves.

Introduction

Extensive experimental research work has been carried out over the last several years to develop an Mg-based alloy with enhanced properties at elevated temperatures. Various studies were made in order to find additional elements to improve the castability and creep resistance at elevated temperatures. Previous research on Mg–Zn–Sn and Mg–Zn–Sn–Ca alloys has shown that Zn improves the castability and has several stable intermetallics with Mg, Sn forms the stable Mg_2Sn compound [1], Ca behaves as a grain refiner [2], and creates the stable intermetallic Mg_2Ca [3]. Theoretical description of the precipitation and hardening processes in these alloys may assist in finding their optimal compositions and heat treatments for achieving the required mechanical properties. Models for precipitation kinetics were developed and calibrated for Cu–Ti [4, 5] and Al-based alloys [6, 7]. The microstructure evolution of an Mg–Zn–Sn alloy recently studied by combining microhardness experiments [8], X-ray diffraction, transmission electron microscopy (TEM) and small angle scattering (SAXS) [9, Rashkova et al. (submitted, 2006)] provided determination of precipitated phases, their volume fraction and size distribution. The aim of the present work is to develop and calibrate a model for precipitation hardening in Mg-based alloys, as different types of precipitates form simultaneously.

The model

The model used in the present work is based on the classical theory proposed by Langer and Schwartz [4] and modified by Kampmann and Wagner [5]. This model takes into account three mechanisms involved in the solid-state decomposition of a supersaturated solid solution taking place during aging: nucleation, growth, and coarsening of precipitates.

It should be noted that in this analytical model droplets of a new phase are considered to be spheres, and no elastic energy or anisotropy of interfacial energy effects

A. Katsman (✉) · S. Cohen · M. Bamberger
Department of Materials Engineering, Technion - Israel Institute of Technology, Technion City, Haifa 32000, Israel
e-mail: akatsman@tx.technion.ac.il

are taken into account. Precipitates in the α-Mg-matrix are often of needle-like shape, as in the case of $MgZn_2$, for example. For such a case, some corrections should be introduced in the model, in particular in the law of steady state growth of precipitates and in the Gibbs–Thomson equation. The coarsening process of the needle-like precipitates may differ from that of equiaxed ones, and is driven by the needles' widths. However, if the average width of needles, w, increases proportionally to their average length, l, an equivalent radius of the droplet, $R_p = (3w^2l/16)^{1/3}$ is proportional to w, and a conception of equivalent radius can be used in the model calculations. Baring in mind this simplification, the following model can be developed.

The rate of homogeneous nucleation of precipitates is determined by the following equation:

$$J_p = ZN_0\beta\exp(-\Delta G_p^*/kT)\exp(-t_w/t), \tag{1}$$

where $\Delta G_p^* = (4\pi/3)(R^*)^2\gamma$ is the formation energy of critical nucleus with radius R^*, as R^* represents the limit above which a particle becomes stable:

$$R^* = \frac{2\gamma V_m}{X_\beta R_g T}\cdot\frac{1}{\ln(X_\alpha/X_e)} \tag{2}$$

$\beta = D_\alpha X_\alpha/a^2$, D_α is the diffusion coefficient of the species responsible for new phase nucleation, a is the atomic jump distance, X_α and X_e are the mean and equilibrium concentrations of the species in the matrix, X_β is the concentration in the precipitate, γ is the surface energy of the nuclei, t_w is the incubation period, Z is the Zeldovich factor, V_m is molar volume of the nucleated phase, k is the Bolzman's constant, R_g is the gas constant, and T is the absolute temperature.

The growth rate of the precipitates is approximated by the steady state solution of the second Fick's law:

$$\frac{dR_p}{dt} = v_p = \frac{D_\alpha}{\varphi\cdot R_p}\cdot\frac{X_\alpha - X_{\alpha/\beta}^{R_p}}{X_\beta - X_{\alpha/\beta}^{R_p}} \tag{3}$$

where R_p is the equivalent radius of the precipitate, $\phi = 1$ for spherical particles and $\phi = \ln(d/w) = (1/3)\ln(\pi\ l/4fw)$ for cylindrical (needle-like) droplets of width w and length l, d being the average distance between needles and f is their volume fraction, $X_{\alpha/\beta}^{R_p}$ is the concentration at the matrix/precipitate interface, as the latter depends on R_p according to Gibbs–Thomson equation:

$$X_{\alpha/\beta}^{R_p} = X_e\cdot\exp\left\{\frac{2\gamma V_m}{R_g T}\cdot\frac{1}{\theta\cdot R_p}\right\}, \tag{4}$$

where θ is the shape dependent parameter; for a sphere shape $\theta = 1$, for needles $\theta = w/2R_p < 1$.

It is assumed in the Langer-Schwartz model that the system contains N_p droplets per unit volume of uniform size $R_p > R^*$; the number of particles is given by integration of equation:

$$\frac{dN_p}{dt} = J_p - f_a(R^*,t)\cdot\frac{dR^*}{dt}, \tag{5}$$

where $f_a(R^*,t)$ is the apparent density of particles:

$$f_a(R^*,t) = N_p\frac{b_{LSW}}{R_p - R^*} \tag{6}$$

$b_{LSW} = 0.317$ is chosen to force the average particle size to tend toward the long time LSW coarsening rate.

The time evolution of the droplet average size, R_p, is described by the following equation:

$$\begin{aligned}\frac{d\bar{R}_p}{dt} &= v_p(\bar{R}_p) + (\bar{R}_p - R^*)\cdot\frac{f_a(R^*,t)}{N_p}\cdot\frac{dR^*}{dt}\\ &\quad + \frac{1}{N_p}J_p(R^*(t))\cdot(R^* + \delta R^* - \bar{R}_p)\end{aligned} \tag{7}$$

The third term in Eq. 7 is concerned with the nucleation of particles slightly larger than those of a critical size, $R = R^* + \delta R^*$, and $\delta R^* \ll R^*$. Here δR^* is a parameter of the model. Equations 5 and 7 should be coupled with the solute conservation equation:

$$\frac{X_{0\alpha} - \bar{X}_\alpha}{X_\beta - \bar{X}_\alpha} = \frac{4\pi}{3}\bar{R}_p^3\cdot N_p^3 \tag{8}$$

In the case of multi-component alloys, different types of precipitates, with different kinetic and thermodynamic parameters, may develop simultaneously. As a result, Eqs. 5–8 should be written for each type of precipitate. It should be noted that the model in the present form may be applied only to the nucleation and growth of binary phases. In the case of Mg–Zn–Sn alloys, two types of binary precipitates, $MgZn_2$ and Mg_2Sn, are assumed to form independently, and the model can describe simultaneous evolution of them both.

Using dimensionless parameters

$$\begin{aligned}&\rho_i = \bar{R}_i/R_{Ni}, \quad \xi_i = \bar{X}_{\alpha i}/X_{ei}, \quad n_i = N_{pi}\cdot\tfrac{4\pi}{3}\cdot R_{Ni}^3,\\ &\tau = D_1 t/R_{N1}^2, \quad \bar{J}_i = J_{pi}\frac{dn_i}{dN_{pi}}\cdot\frac{dt}{d\tau}, \quad k_{\gamma i} = \gamma_i/\gamma_0,\ i = 1,2\end{aligned} \tag{9}$$

where $R_{Ni} = 2V_{mi}\,\gamma_0/(X_{\beta i}\,R_g\,T)$ and γ_0 are the scaling length and interphase surface energy, V_{mi} is the molar volume of

the new phase i, one can obtain a system of four differential equations:

$$\begin{cases} \dfrac{d\rho_1}{d\tau}+\dfrac{\rho_1}{3}\left\{\dfrac{1}{\xi_{01}-\xi_1}+\dfrac{b\cdot k_{\sigma 1}}{\rho_1\cdot\ln\xi_1}\cdot\dfrac{1}{\xi_1\cdot\ln\xi_1}\right\}\cdot\dfrac{d\xi_1}{d\tau} \\ =-\bar{J}_1\cdot\dfrac{\rho_1^4}{3}\cdot\dfrac{\xi_{p1}-1}{\xi_0-\xi_1} \\ \dfrac{d\rho_1}{d\tau}+\dfrac{b\cdot k_{\sigma 1}}{\xi_1(\ln\xi_1)^2}\cdot\dfrac{d\xi_1}{d\tau}=\dfrac{1}{\xi_{p1}-1}\cdot\dfrac{1}{\rho_1}\cdot\left\{\xi_1-\exp\left(\dfrac{k_{\sigma 1}}{\rho_1}\right)\right\} \\ +\rho_1^3\cdot\dfrac{\xi_{p1}-1}{\xi_{01}-\xi_1}\cdot\bar{J}_1\cdot\left[\dfrac{k_{\sigma 1}}{\ln\xi_1}+\delta\rho^*-\rho_1\right] \\ \dfrac{d\rho_2}{d\tau}+\dfrac{\rho_2}{3}\left\{\dfrac{1}{\xi_{02}-\xi_2}+\dfrac{b\cdot k_{\sigma 2}}{\rho_2\cdot\ln\xi_2}\cdot\dfrac{1}{\xi_2\cdot\ln\xi_2}\right\}\cdot\dfrac{d\xi_2}{d\tau} \\ =-\bar{J}_2\cdot\dfrac{D_2}{D_1}\cdot\dfrac{\rho_2^4}{3}\cdot\dfrac{\xi_{p2}-1}{\xi_{02}-\xi_2} \\ \dfrac{d\rho_2}{d\tau}+\dfrac{b\cdot k_{\sigma 2}}{\xi_2(\ln\xi_2)^2}\cdot\dfrac{d\xi_2}{d\tau}=\dfrac{1}{\xi_{p2}-1}\cdot\dfrac{1}{\rho_2}\cdot\left\{\xi_2-\exp\left(\dfrac{k_{\sigma 2}}{\rho_2}\right)\right\} \\ +\rho_2^3\cdot\dfrac{\xi_{p2}-1}{\xi_{02}-\xi_2}\cdot\bar{J}_2\cdot\dfrac{D_2}{D_1}\cdot\left[\dfrac{k_{\sigma 2}}{\ln\xi_2}+\delta\rho^*-\rho_2\right] \end{cases} \tag{10}$$

The conservation conditions in a dimensionless form complete this system of equations:

$$n_i=\frac{1}{\rho_i^3}\cdot\frac{\xi_{0i}-\xi_i}{\xi_{pi}-1},\quad i=1,2 \tag{11}$$

The set of Eq. 10 were solved numerically by using a fourth-order Runge-Kutta method, using Eq. 11 to compute the dimensionless density of precipitates. Different parameters of $k_{\gamma 1}$ and $k_{\gamma 2}$, the ratio of diffusivities D_2/D_1 and different initial supersaturations ξ_i were used in the calculations. Incubation periods in the scaled version were estimated as

$$\begin{aligned} \tau_{w1} &= \tfrac{1}{2}(\rho*)^2 c_{w1}^2\tfrac{\xi_{p1}-1}{\xi_{01}-1}\equiv\tau_{w1,\min}c_{w1}^2, \\ \tau_{w2} &= \tfrac{1}{2}(\rho^*)^2 c_{w2}^2\tfrac{\xi_{p2}-1}{\xi_{02}-1}\tfrac{D_1}{D_2}\equiv\tau_{w2,\min}c_{w2}^2 \end{aligned} \tag{12}$$

derived from the assumption that the minimum time, $\tau_{w,min}$, for a particle to reach the critical size ρ^* is given by Eq. 3 with $X_{\alpha/\beta}^{R_p}=X_e$. The latter equation usually overestimates the growth rate of subcritical nuclei (since $X_{\alpha/\beta}^{R_p}>X_e$) , and it is counterbalanced by the parameters c_{wi}, which are determined by fitting of results with experimental data. Typical variations of precipitates' dimensionless densities and average radius as a function of a dimensionless time are shown in Figs. 1 and 2. The values used for the calculations are given in the figure captions. As can be seen, the height and width of the density peak are very sensitive to the dimensionless surface energy k_γ (Fig. 1a). Its location depends on the incubation time

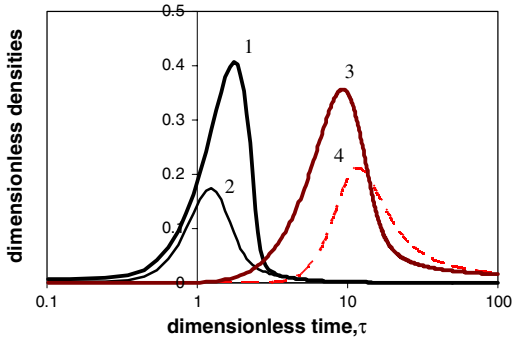

Fig. 1 Calculated dimensionless densities of precipitates as a function of a dimensionless ageing time of supersaturated alloy; curves 1,2 – n_1 for supersaturation ξ_{01} = 1.6 and interfacial energies $k_{\gamma 1}$ = 0.06 (1) and $k_{\gamma 1}$ = 0.08 (2); curves 3,4 – n_2 for $k_{\gamma 2}$ = 0.5, D_2/D_1 = 0.084 and supersaturations ξ_{02} = 9 (3) and ξ_{02} = 5 (4)

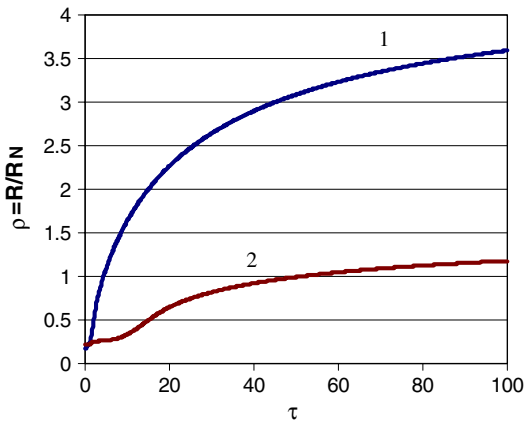

Fig. 2 Calculated average normalized radii of two kinds of precipitates as a function of the dimensionless time; 1–$\rho_1 = R_1/R_N1$ for ξ_{01} = 1.6, $k_{\gamma 1}$ = 0.08; 2–$\rho_2 = R_2/R_N2$ for ξ_{02} = 9, $k_{\gamma 2}$ = 0.5, D_2/D_1 = 0.084

(Fig. 1b), which, in turn, depends on corresponding initial supersaturation and interface energy. Shape dependent parameters, ϕ and θ, may change the effective diffusion coefficients and surface energies: $D' = D/\phi$ and $\gamma' = \gamma/\theta$, that should be taken into account in the analysis of calculation results.

Precipitation hardening due to particle-dislocation interaction

Hardening during aging of supersaturated alloys is determined by precipitates-dislocation interaction. Coherent precipitates, depending on their size and spacing, can be sheared or bypassed by dislocations [10]. When the precipitates are sheared, the stress at which the particles are overcome is proportional to their average size and inversely proportional to the effective distance between particles along a dislocation line, λ:

$$\sigma_{sh} = \Gamma_1 \frac{\bar{R}_p}{\lambda}, \tag{13}$$

where Γ_1 depends on the nature of the interaction between precipitates and dislocations, as well as on the type of dislocation, $\Gamma_1 = 2\gamma_a/b$, γ_a represents the force per unit length opposing the motion of dislocation as it penetrates the particle, whereas b is the Burgers vector. In the following consideration Γ_1 was assumed as a parameter averaged over all types of dislocations interacted with precipitates. Taking into account a relationship between λ and the square lattice spacing, λ_s, between obstacles in the glide plane [11]: $\lambda = \lambda_s/\beta_c^{1/2}$, where $\beta_c = \Gamma_1 b\bar{R}_p/2\Gamma$, one can obtain:

$$\sigma_{shear} = \tilde{\Gamma}\frac{\bar{R}_p^{3/2}}{\lambda_s} \tag{13a}$$

where $\tilde{\Gamma} = \Gamma_1^{3/2}(b/2\Gamma)^{1/2}$, Γ is the dislocation line tension. When the precipitates increase in size, and the distance between precipitates also increases, it becomes easier for the dislocation to bypass them. In this case the strengthening depends only on the distance between precipitates in the glide plane λ_s and on the dislocation line tension, according to Orowan equation [12, 13]:

$$\sigma_{by-pass} = 0.81\frac{2\Gamma}{b\lambda_s} \tag{14}$$

This prevails for precipitates having a radius higher than a critical value, $\bar{R}_C$ given by the equality of two stresses $\sigma_{shear} = \sigma_{by\text{-}pass}$:

$$\bar{R}_C = 1.74\frac{\Gamma}{b\Gamma_1} = 0.87\frac{\Gamma}{\gamma_a} \tag{15}$$

Two strengthening mechanisms associated with particle-dislocation interaction (shearing and bypassing) should be considered as operating simultaneously due to particle size-distribution, $f(\bar{R}_p)$. The contribution of precipitates sheared by dislocations to hardness can be written as follows [6]:

$$\sigma_i^{shear} = \frac{\tilde{\Gamma}_i}{\lambda_{si}}\int_0^{\bar{R}_{Cii}} R_p^{3/2}\cdot f_i(R_p)\mathrm{d}R_p \quad i = 1,2 \tag{16}$$

and the contribution of by-passed precipitates as:

$$\sigma_i^{by-pass} = \frac{1.64\Gamma\cdot\bar{R}_{Ci}}{b\lambda_{si}}\cdot\int_{\bar{R}_{Ci}}^{\infty} f(R_p)\mathrm{d}R_p \quad i = 1,2 \tag{17}$$

In the case of two kinds of precipitated phases, the total contribution of four sets of discrete obstacles to precipitation hardening can be evaluated according to different rules mentioned in the literature (e.g., [11, 14]). Computer simulation [15] and theoretical investigations [16] have shown that the so-called Pythagorean addition rule is the best approximation for the case of distinct obstacles of two or more strengths. In the present consideration the precipitation hardening can be estimated as:

$$\Delta\sigma_{prec} = \sqrt{(\sigma_1^{shear})^2 + (\sigma_2^{shear})^2 + (\sigma_1^{by-pass})^2 + (\sigma_2^{by-pass})^2} \tag{18}$$

For the size distribution, $f(R_p)$, as suggested by Deschams and Brechet [6], the Gaussian law was used:

$$f(R_p) = \frac{2}{\Delta\sqrt{\pi}}\cdot\frac{1}{1+erf(\bar{R}_p/\Delta)}\cdot\exp\left[-\frac{(R_p-\bar{R}_p)^2}{\Delta^2}\right] \tag{19}$$

$\bar{R}_{Ci}, \tilde{\Gamma}_i$ and Δ will serve as the fitting parameters of the hardening model. For particle spacing, λ_s, the expression of Kocks, obtained on the basis of computer simulations [14] was used:

$$\lambda_s = 1.15\sqrt{\frac{2\pi}{3\cdot f_v}}\cdot\bar{R} \tag{20}$$

where f_v is the particle volume fraction and $\bar{R}$ is the overall average radius of precipitates.

The strengthening of the alloy is usually considered as the result of a mixture of different contributions [14]:

$$\sigma_{tot} = \sigma_0 + \sigma_{sol} + \Delta\sigma_{prec} \tag{21}$$

where σ_0 is the friction stress of the matrix, σ_{sol} is the solid solution contribution; it is usually calculated as:

$$\sigma_{sol} = K_i X_i^{2/3}, \tag{22}$$

where X_i are the concentrations of impurities in the matrix. In our calculations, σ_0 was considered constant. The contribution of the solid solution strengthening can be evaluated using the difference in hardness between the alloyed and pure magnesium, $\sigma_{tot}^0 - \sigma_{tot}^0$ (pure) $= \sigma_{sol}^0 = K_i X_{0i}^{2/3}$. Assuming that the microhardness of the alloy is proportional to the total stress, σ_{tot}, the relative change in the microhardness during precipitation can be found as:

$$\frac{H_{tot}-H_0}{H_0} = \frac{\Delta\sigma_{prec} - K_i(X_{0i}^{2/3} - X_i^{2/3})}{\sigma_0 + K_i X_{0i}^{2/3}} \tag{23}$$

Experimental results and discussion

Mg–Zn–Sn alloy with 4.53 wt.% Zn and 4.75 wt.%Sn was solution treated at 465 °C for 96 h and then water quenched. Aging at 175, 200, 225, and 250 °C up to 96 h has

led to the precipitation of the binary phases $MgZn_2$ and Mg_2Sn. The formation of these phases was studied experimentally. The two maxima during aging were found to be related to the formation of two types of precipitates, which were detected by XRD and SEM investigations: the first is $MgZn_2$ and the second is Mg_2Sn [8].

TEM investigations revealed that Mg_2Sn particles are plate-like and mainly equiaxed in the α-Mg-matrix while precipitates of $MgZn_2$ have a needle-like shape and are semi-coherent during almost all stages of growth and coarsening [9], so internal stress due to misfit strains may influence their kinetics of coarsening. Such influence can be substantial if the ratio of elastic and interfacial energies, measured by the dimensionless parameter $\hat{S} = \varepsilon^2 L C_{44}/\gamma$, is more than 4.5 [17, 18], where ε is the particle-matrix misfit, L is a characteristic length, e.g. an equivalent radius of a particle, C_{44} is an elastic constant and γ is the interfacial energy. Evaluation of this parameter for $MgZn_2$-precipitates embedded in the Mg-matrix in such a way that the $\{11\bar{2}0\}_{MgZn2}$ lattice planes are parallel to the $(0002)_{\alpha\text{-Mg}}$ planes (which is the case realized [9]), for ε = 0.04 [Rashkova et al. (submitted, 2006)], C_{44} = 16.4 GPa [19], assuming L = 100 nm and γ = 10 mJ/m^2 yields $\hat{S} \approx 0.26$. Thus, in this case, a coarsening process can be considered as stress-free for $MgZn_2$ as well as for Mg_2Sn-precipitates which are incoherent in the α-Mg-matrix.

The variation in the measured hardness with time is given in Fig. 3. The solid curves correspond to the calculated values. Precipitation hardening gives the main contribution to the results. The variation in solid solution strengthening was evaluated by comparison with the hardness of pure magnesium that undergone the same thermal treatment. It was found that this variation is small

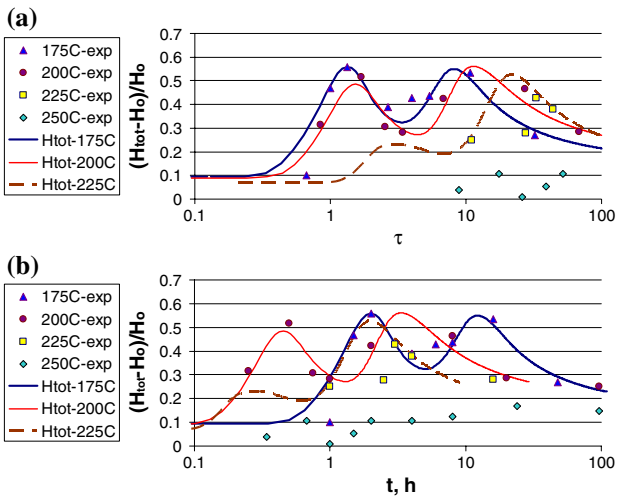

Fig. 3 Precipitation hardening of water quenched Mg–Zn–Sn alloys as a function of the dimensionless (**a**) and dimensional (**b**) ageing time at different temperatures. Parameters used in calculations are present in the Table 1, scaling parameters t/τ—in Table 2

and can be neglected in the present analysis. The simulation parameters $k_{\gamma 1}$ and $k_{\gamma 2}$ were chosen by fitting the shapes of the calculated relative microhardness peaks, Eqs. 17–23, with experimental microhardness maxima corresponding to the evolution of given precipitates [8, 9] (Fig. 3); the location of peaks on the dimensionless time axis is determined by parameters c_w1, c_w2 and D_2/D_1. Additional temperature dependence of results is connected with variations in the limit solubilities, hence in the initial supersaturations ξ_{0i} (see Table 1). Experimental alloy's concentrations, $X_{0,Zn}$ = 1.7 at.% and $X_{0,Sn}$ = 1.0 at.%, and the limit solubilities of Zn and Sn in Mg taken from the Mg–Zn and Mg–Sn phase diagrams were used to obtain the initial supersaturations, $\xi_{01} = X_{0,Zn}/X_{e,Zn}$ and $\xi_{02} = X_{0,Sn}/X_{e,Sn}$. The chosen values $c_w1 = c_w2 = 1.4$ correspond to incubation times $\tau_i \approx 2\tau_{i,min}$ needed to first particles of $MgZn_2$ and Mg_2Sn to become 'observaible'. The parameters found are given in Table 1.

Critical values $\rho_{Ci} = \bar{R}_{Ci}/R_{Ni}$, determining the transition from shearing to bypassing strengthening mechanism were chosen as 0.20 and 0.22 for $i = 1$ and $i = 2$ respectively that gives the best fitting with the initial growth of the hardness peaks ($\sigma \sim f^{1/2}\bar{R}_p^{1/2}$) followed by a behavior that corresponds with the bypassing mechanism ($\sigma \sim f^{1/2}/\bar{R}_p \sim 1/\lambda_s$). So, the latter mechanism prevails during most of the growth period of precipitates. Unfortunately, direct experimental examination of mechanisms responsible for different stages of precipitation hardening in the Mg-based alloys was not done, and it requires a special TEM investigation which is out of the scope of the present work.

The calculated density and average size of precipitates correspond to experimental values according to Eq. (9). Using the available experimental data on volume fractions of $MgZn_2$-precipitates, found by SAXS (Fig. 4) and comparing it with the calculated volume fraction $f_1 = n_1\rho_1^3$, one can find the scaling ratio $(t/\tau) = R_{N1}^2/D_1$. The average needle's size evolution (Fig. 5, [Rashkova et al.

Table 1 Parameters used in calculations of the relative microhardness change.

T (°C)	175	200	225
$X_{e,Zn}$ (at.%)	1.07	1.12	1.34
$X_{e,Sn}$ (at.%)	0.11	0.12	0.13
ξ_{01}	1.59	1.52	1.27
ξ_{02}	9.1	8.3	7.7
D_2/D_1	0.064	0.060	0.062
c_w1	1.4		
c_w2	1.4		
$k_{\gamma 1}$	0.08		
$k_{\gamma 2}$	0.50		

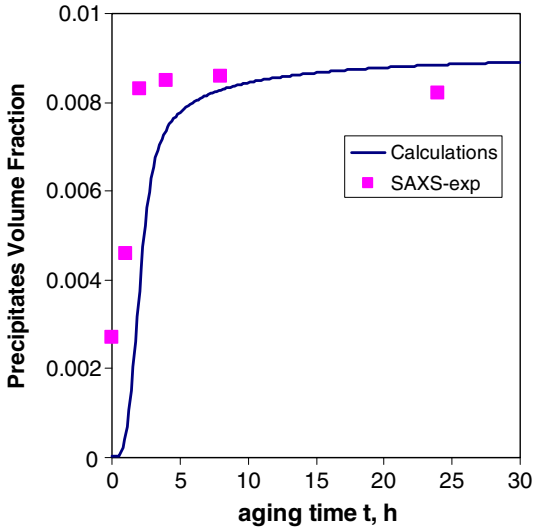

Fig. 4 Variation in the volume fraction of $MgZn_2$-precipitates during aging at 175 °C; parameters used in calculations are present in Tables 1, 2. Comparison of experimental results [Rashkova et al. (submitted, 2006)] with calculated ones (solid line) allows finding the ratio $t/\tau = R_{N1}^2/D_1 = 1.5$ h

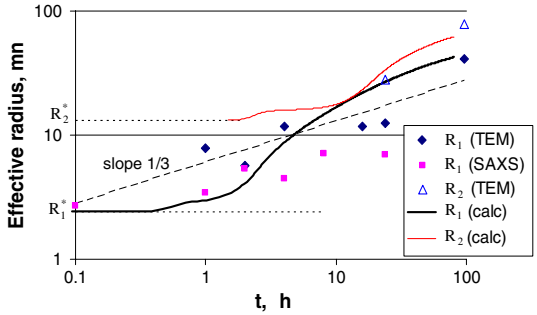

Fig. 5 Variation in the effective radius of $MgZn_2$(R_1) and Mg_2Sn (R_2) precipitates during aging at 175 °C of the quenched alloy Mg–Zn–Sn [9, Rashkova et al. (submitted, 2006)] and calculated values $R_1 = \rho_1 R_{N1}$ and $R_2 = \rho_2 R_N2$ with $R_N1 = 14$ nm, $R_N2 = 62$ nm, $R_1^* = R_N1/\ln \xi_{01} = 2.4$ nm and $R_2^* = R_N2/\ln \xi_{02} = 13.2$ nm

(submitted, 2006)]), allows finding the scaling lenghts R_{Ni} which were evaluated as follows: $R_{N1} \approx (6.2/T)$μm and $R_{N2} = (V_{m2}\, X_{\beta 1}/V_{m1}\, X_{\beta 2})R_{N_1} \approx (27.4/T)$μm (Table 2). On the other hand, by using the values of molar volumes $V_m1 = 2.1\cdot10^{-5}m^3$, $V_m2 = 4.65\cdot10^{-5}m^3$ for $MgZn_2$ and Mg_2Sn respectively, the value of the scaling surface energy, γ_0, can be evaluated as: $\gamma_0 = (R_{Ni}\, X_{\beta i}\, R_g\, T)/2V_{mi} \approx 0.82$ J/m^2. The corresponding surface energies of the nuclei are as follows: $\gamma_1 = \gamma_{MgZn_2} = k_{\gamma 1}\, \gamma_0 \approx 0.065$ J/m^2 and $\gamma_2 = \gamma_{Mg_2Sn} = k_{\gamma 2}\, \gamma_0 \approx 0.41$ J/m^2 (Table 2). The low value of interface surface energy, γ_1, is in line with the coherent interface between $MgZn_2$ precipitates and Mg-matrix. A rather large value of γ_2 is indicative of incoherent interfaces between Mg_2Sn-particles and Mg.

The experimental times, $t_{ml} = \tau_{ml} R^2_{N_1/D_1}$, elapsed before the first maximum strength is achieved, and the ratios D_2/D_1 were used to determine the effective diffusion coefficients D_1 and D_2 responsible for the precipitates formation process (see Table 2). Comparison of these values with diffusion coefficients of Zn and Sn in Mg, $D_{Zn} = 1.05\exp(-125.8$ kJ/RT)cm^2/s [20] and $D_{Sn} = 4.27\exp(-149.6$ kJ/RT)cm^2/s [21] extrapolated from high temperatures (Fig. 5) shows that D_1 is about $3 \div 4$ times smaller than D_{Zn}. The decreasing parameter ϕ introduced in Eq. 3 can be estimated as $(2.0 \div 2.4)$ for measured volume fractions of the needles $f = (0.4 \div 0.8)\%$ and the aspect ratio l/w found for the $MgZn_2$-needles as $4 \div 8$ [9, Rashkova et al. (submitted, 2006)]. Decrease in the effective diffusion coefficient may be related to the absorption of Zn-atoms, mainly by incoherent needle tips that reduces the diffusion flux by the factor l/w. It can be also connected with compressive coherent stresses near the tips and tensile stresses along the needles so that small Zn-atoms are directed to the needle tips. It should be noted that the formation of the

Table 2 Physical parameters evaluated from calculations compared with experimental data

T (°C)	175	200	225
R_N1 (nm)	14 ± 4	13.2 ± 3.8	12.6 ± 3.6
R_N2 (nm)	62 ± 17	58 ± 16	56 ± 16
R_1^* (nm)	2.4 ± 0.7	2.5 ± 0.7	3.0± 0.9
R_2^* (nm)	13.2 ± 3.6	13.7 ± 3.8	13.7 ± 3.9
D_1 (10^{-20}m^2/s)	7.4 ± 3.8	33 ± 7	159 ± 74
D_2 (10^{-20}m^2/s)	0.5 ± 0.2	1.9 ± 0.4	10.0± 4.4
t/τ (h)	0.8 ± 0.1	0.15 ± 0.03	0.03 ± 0.01
t_w1 (h)	2.4 ± 0.3	0.6 ± 0.05	0.5 ± 0.05
t_w2 (h)	15.6 ± 1.9	5.6 ± 0.4	3.8 ± 0.8
γ_1^2 (mJ/m)	65 ± 18		
γ_1^2 (mJ/m)	410 ± 120		
γ_a1 ($^2_{mJ/m}$)	55 ± 13		
γ_a2 ($^2_{mJ/m}$)	12 ± 3		

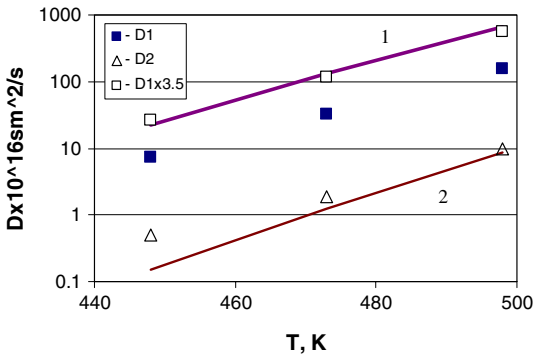

Fig. 6 Calculated effective diffusion coefficients D_1 and D_2 responsible for evolution kinetics of $MgZn_2$ and Mg_2Sn precipitates; 1—$D_{Zn} = 1.05\exp(-125.8\ \text{kJ/RT})\text{cm}^2/\text{s}$ [20] and 2–$D_{Sn} = 4.27\exp(-149.6\ \text{kJ/RT})\text{cm}^2/\text{s}$ [21]

$MgZn_2$-phase in the Mg-matrix occurs with substantial decrease in the average atomic volume: $\bar{v}_a(MgZn_2) = 1.16 \cdot 10^{-29}\,\text{m}^3$ and $\bar{v}_a(Mg) = 2.32 \cdot 10^{-29}\,\text{m}^3$ and should be accompanied by the formation of vacancies. The coefficient D_2 is close to D_{Sn} yet slightly higher. It is possibly caused by increased vacancy concentration mentioned before. With this in mind one can conclude that the first maximum is actually related to the precipitation of $MgZn_2$, and the second is related to Mg_2Sn precipitation.

Using scaling lengths R_{Ni}, one can evaluate critical radii $\bar{R}_{C_i} : \bar{R}_{C1} \approx 2.8\,\text{nm}$ and $\bar{R}_{C2} \approx 13.6\,\text{nm}$ and the corresponding surface energies $\gamma_a = 1.87 \cdot \Gamma/\bar{R}_C$. Assuming $\Gamma \approx Gb^2/2$, $G = C_{44} = 16.4$ GPa, $b = (1/3)a_{Mg} = 0.1$ nm, one can find $\gamma_{a1} \approx 55\ \text{mJ/m}^2$ and $\gamma_{a2} \approx 12\ \text{mJ/m}^2$ (Table 2). These values may correspond to energies of antiphase boundaries formed by dislocations penetrating the precipitated ordered phases, or to a difference in the stacking fault energies between the matrix and precipitates. Further detailed investigation of the hardening mechanisms in Mg-based alloys is required to resolve this question.

Thus, a reasonable agreement between calculated and experimental precipitation hardening was found for the temperatures 175 and 200 °C. For higher temperatures, 225 and 250 °C, the first maximum was not detected, apparently because of very short aging times when it appears at such temperatures. The measured values of hardness at the second maximum are lower (especially for 250 °C) than the calculated ones. One can assume that these deviations are connected with a recrystallization process occurring at such high temperatures, which are above $0.5T_{melt}$, where T_{melt} is the alloy melting temperature.

Conclusion

The model for the precipitation and hardening processes in Mg-based alloys was developed on the basis of modified Langer-Schwartz approach. Analysis of the evolution and precipitation hardening of precipitates during the aging of Mg–Zn–Sn alloy was carried out while taking into account the simultaneous formation of the binary $MgZn_2$ and Mg_2Sn phases. Two strengthening mechanisms associated with particle-dislocation interaction (shearing and bypassing) were considered as operating simultaneously due to particle size-distribution. A reasonable agreement between the calculations and observations was found.

The scaling parameters of the model, R_{Ni} and γ_0, were found by fitting the calculated densities and average size of precipitates with the measured ones. Interface surface energies, γ_1 and γ_2, and effective diffusion coefficients responsible for the strengthening kinetics, D_1 and D_2, were estimated based on the microhardness experiments. Two maxima of hardness during aging were found to be related to the formation and coarsening of two types of precipitates, $MgZn_2$ and Mg_2Sn. The values of γ_1 and γ_2 are in line with the nucleation of coherent $MgZn_2$-particles and incoherent Mg_2Sn-particles. Effective diffusion coefficients correspond to the solute diffusion of Zn and Sn in Mg but can be affected by the features of the new phase particles: in the case of $MgZn_2$-needles, D_1 is reduced by the factor l/w in comparison with the usual bulk diffusion coefficient D_{Zn}.

The transition from shearing to bypassing strengthening mechanism was found to occur at rather early stages of the particle growth. The bypassing was found to be the prevailing strengthening mechanism in the investigated alloys. The model allows the description of competitive hardening mechanisms taking into account the distribution of precipitate size and strength as well as the transition from one mechanism to another. However, additional investigations are required to identify these mechanisms.

Acknowledgements The study was partially supported by the B. and N. Ginsburg Research Fund and German Israeli foundation for scientific research and development (GIF) under contract number I-704–43.10/2001. The foundations are acknowledged for their support.

References

1. Mabuci M, Higashi K (1996) Acta Mater 44:4611
2. Nie JF, Muddle BC (1997) Scripta Mater 37:1475
3. Rokhlin LL, Nikitina NI (1998) J Alloys and Compounds 279:166
4. Langer JS, Schwartz AJ (1980) Phys Rev A 21:948
5. Kampmann R, Wagner R (1984) In: Haasen P, Gerold V, Wagner R, Ashby MF (eds) Proceedings of the 2nd Acta-Scripta Metallurgica Conference. Decomposition of alloys: the early stages. Pergamon Press, Oxford, p 91
6. Deschamps A, Brechet Y (1999) Acta Mater 47(1):293
7. Gandin ACh, Brechet Y, Rappaz Canova MG, Ashby M, Shercliff H (2002) Acta Mater 50:901
8. Cohen S, Goren-Muginstein GR, Avraham S, Rashkova B, Dehm G, Bamberger M (2005) Z Metallkd 96:1081

9. Rashkova B, Cohen S, Goren-Muginstein G, Bamberger M, Dehm G (2005) Analytical and high resolution TEM analysis of precipitation hardening in Mg-Zn-Sn alloys, 7th Multinational Congress on Microscopy, Portoroz, Slovenia, p 183
10. Gerold V (1979) In: Nabarro FRN (ed) Precipitation hardening, Dislocations in solids, Vol 4. Van Nostrand, p 219
11. Ardell AJ (1985) Metal Trans 16A:2131
12. Orowan E (1948) Symposium on Internal Stresses in Metals and Alloys, Session III Discussion, Institute of Metals, London, England, p 451
13. Foreman AJE, Makin MJ (1966) Phil Mag 14:911
14. Kocks UF, Argon AS, Ashby MF (1975) Prog Mater Sci 19:1
15. Foreman AJE, Makin MJ (1967) Can J Phys 45:511
16. Hanson K, Morris JW (1975) J Appl Phys 46:2378
17. Thomson ME, Su CS, Voorhees PW (1994) Acta Metall Mater 42:2107
18. Thornton K, Akaiwa N, Voorhees PW (2003) Preprint submitted to Elsevier Science
19. Brandes EA, Brook GB (eds) (1992) Smithells Metals Reference Book 7th edition. Butterworth-Heinemann Ltd, Linarce House Jordan Hill Oxford OX2 8DA
20. Cermak J, Stloukal I (2006) Phys Status Solidi 203a:2386
21. Combronde J, Brebec G (1972) Acta Met 20:37